2026 IEEE International Conference on Robotics and Automation (ICRA 2026)
June 1-5, 2026. Vienna, Austria

Robotic Cell Manipulation at the Solid-Liquid Interface for Cryopreservation

Aojun Jiang[1], Han Yang[2,3], Haocong Song[1], Wenyuan Chen[1], Yu Sun[1,*], and Zhuoran Zhang[2,3,*]

***Abstract*— Automating cell manipulation at a solid-liquid interface is a critical challenge for biomedical applications such as embryo cryopreservation. Unlike manipulation in a full liquid medium, the cell-substrate contact creates a significant static friction force that is not readily measurable with current sensing or vision technologies. This unpredictability poses a high risk of cell loss, as the cell can transition abruptly from a static to a high-velocity state when the applied hydrodynamic force breaches the friction threshold. Existing methods fail to estimate this hidden friction parameter and cannot anticipate the sudden dynamic shift. To address this challenge, this paper proposes a worst-case predictive control approach with online adversarial parameter estimation (WPC-OAPE). The core innovation is the inference of the static friction barrier from observations made while the cell is still stationary. This estimate then informs a predictive controller that proactively plans against the worst-case scenario, to select the optimal action. The WPC-OAPE scheme was validated in robotic embryo vitrification experiments, where it achieved a 100% success rate with zero cell loss. This performance significantly surpassed open-loop (66.6% success) and standard predictive control (83.3% success) methods, proving its potential for clinical applications.**

I. Introduction

Robotic cell manipulation has been applied to various biomedical applications, demonstrating high consistency and efficiency over manual operations [1]. These applications range from high-throughput tasks such as drug screening [2] to high-precision procedures such as tissue engineering [3], single-cell analysis [4], and intracytoplasmic sperm injection [5]. A common characteristic of these tasks is the manipulation of cells fully suspended in a liquid medium. Consequently, the control objective is to regulate the hydrodynamic forces between the cell and the fluid, and existing control schemes are primarily designed for this context.

However, many biomedical applications require cell manipulation at a solid-liquid interface instead of in a pure liquid environment. Manipulation at a solid-liquid interface introduces complex physical dynamics, such as friction, not present in pure liquid systems and thus not addressed by existing control schemes. These applications span from basic research on cell-substrate adhesion [6] to clinical applications such as the selection of specific cell colonies [7] and single-cell surgery [8]. A representative example is the vitrification of human oocytes and embryos for cryopreservation, which is a widely adopted and increasingly demanded procedure in assisted reproductive technology [9]. Vitrification provides an effective measure to preserve reproductive capability for medical or social reasons [10] via preserving samples in liquid nitrogen. The success of vitrification has also enabled advanced treatments, including preimplantation genetic testing [11] and delayed embryo transfer [12]. A key step in vitrification involves using a micropipette to remove excess cryoprotectant solution from a cell resting on a cryo-carrier substrate, as shown in Fig. 1a. This action is essential for achieving the ultra-high cooling rates (e.g., 20,000°C/min [13]) required to prevent ice crystal formation and ensure cell viability [14].

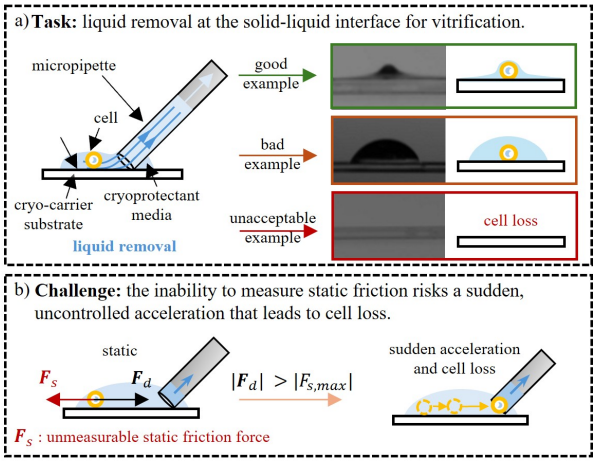

Fig. 1. Schematics of a cell manipulation task at the liquid-solid interface and its challenge. (a) During vitrification, excessive cryoprotectant media around the cell needs to be removed via micropipette aspiration. (b) During the removal of the excessive media, a drag force is exerted on the cell. A unmeasurable static friction force balances this force if the cell remains static. Under such uncertainty, when the drag force surpasses the maximum static friction force, there is a high risk of sudden acceleration of the cell towards the pipette tip, leading to cell loss.

A major concern for cell manipulation at a solid-liquid interface is cell loss [15]. Still taking vitrification as an example, during the liquid removal step, aspiration from the micropipette creates a hydrodynamic drag force on the cell, which is opposed by static friction from the substrate. If the applied drag force exceeds this static friction threshold, the cell transitions abruptly from a static to a kinetic state. This sudden acceleration can propel the cell uncontrollably towards the pipette, leading to cell loss, as shown in Fig. 1b.

[1]Department of Mechanical and Industrial Engineering, University of Toronto, Toronto, Canada;[2]Institute of Robotics and Intelligent Systems, Dalian University of Technology, Dalian, China;[3]School of Science and Engineering, The Chinese University of Hong Kong, Shenzhen, Shenzhen, China. *Corresponding authors: Zhuoran Zhang (zhangzhuoran@cuhk.edu.cn), Yu Sun (yu.sun@utoronto.ca).

This work was supported in part by National Key R&D Program of China (2023YFE0205500), in part by the National Natural Science Foundation of China (The Science Fund for Excellent Research Groups, 62588301), in part by the Fundamental and Interdisciplinary Disciplines Breakthrough Plan of the Ministry of Education of China (JYB2025XDXM117), and in part by Guangdong Basic and Applied Basic Research Foundation (2024A1515010160).

Cell loss is an unacceptable outcome because human oocytes and embryos are often irreplaceable and extremely limited in number. For the patient, this loss can represent a profound emotional and financial setback, potentially jeopardizing their opportunity to have a biological child.

To prevent cell loss, an effective strategy is to regulate the applied force if the opposing friction is measurable. However, measuring this static friction is a fundamental challenge. Force feedback in micromanipulation is typically achieved through two approaches. The first approach is direct sensing, which utilizes instruments like AFM cantilevers [16], optical tweezers [17], or end-effector-integrated MEMS sensors [18] to measure interaction forces. However, the static friction originates at the cell-substrate interface and is misaligned with force sensors on the micropipette end-effector. Moreover, the use of disposable substrates in clinical settings makes the integration of sensors economically infeasible. The second approach, vision-based force inference, estimates forces from image data. This is done by tracking the deformation of a calibrated flexible tool [19], measuring cell membrane strain [20], or analyzing fluid tracers (e.g., micro-PIV [21]). While useful for dynamic events, this method is unable to quantify static friction. Because a stationary cell undergoes no motion or deformation, vision can confirm the cell's immobility but cannot determine its static friction threshold. Therefore, measuring the static friction force is not feasible with either direct sensing or vision-based methods.

Without measuring friction forces, one control strategy is open-loop control, which aims to passively increase friction through means such as modifying cryo-carrier surface properties [22] or standardizing liquid dispensing protocols [23]. This approach lacks robustness because cell-substrate friction is highly sensitive to uncontrollable variations in liquid volume, surface properties, and intrinsic cell adhesion [24]. Another existing control strategy is reactive control [25], which employs vision to trigger a retreat maneuver after the cell begins to move. The primary limitation of this method is system latency. The transition from static to kinetic friction is often abrupt and can induce high acceleration, meaning cell loss may occur before the system can respond.

Predictive controllers [26][27] have been developed to overcome latency using a dynamic model to forecast future states. However, current implementations are not designed for cell manipulation at the solid-liquid interface. Therefore, the characteristics of cell-substrate friction are not adequately modelled. Their predictions are based on the cell's current state. When the cell is stationary, existing models predict it will remain stationary, failing to anticipate the sudden impulse when the friction threshold is breached. Although predictive in architecture, the controller's awareness of the failure (e.g., cell loss) is still retrospective. This cognitive lag in its model renders it ineffective against the rapid, unmodeled dynamics of the transition.

To automate this task safely and robustly, what is needed is a control method that can overcome this predictive impasse and achieve the following two objectives:

1) To estimate the static friction using observations made while the cell is still stationary; 2) To determine the optimal motion and aspiration rate based on this estimate to minimize the risk of cell loss while ensuring task efficiency.

To address these challenges, this paper introduces a novel control scheme: Worst-Case Predictive Control with Online Adversarial Parameter Estimation (WPC-OAPE). We formulate a switched physical model that explicitly captures the bifurcation of cell dynamics, characterized by key adversarial parameters: the static friction barrier and the kinetic friction coefficient. An Extended Kalman Filter (EKF) is developed that maintains a probabilistic belief over these parameters. Crucially, it estimates friction using both direct measurements from motion events and indirect, inequality-based information from static observations and hydrodynamic modelling. Based on this belief, a predictive control law computes actions against a pessimistic, worst-case prediction of the cell's future state. The proposed WPC-OAPE is validated in real-world embryo vitrification experiments, demonstrating robust and efficient fluid removal while respecting uncertain, unmeasurable frictional forces.

II. Problem Formulation

The objective of this robot control problem is to determine the optimal control command $\boldsymbol{u}(t)$, comprising the pipette tip's velocity $\boldsymbol{u}_p(t) = \dot{\boldsymbol{s}}_p(t)$ and the aspiration flow rate $Q(t)$, to manipulate a cell at a solid-liquid interface for vitrification. The control commands generate a micropipette trajectory and a flow rate sequence. This command should be derived from an estimation of the governing friction forces to minimize the risk of cell loss while maximizing task efficiency. The system's known states include the cell position $\boldsymbol{s}_c(t)$ and pipette position $\boldsymbol{s}_p(t)$, available from vision and encoders.

The central challenge lies in the unpredictable nature of the static friction force between the cell and the substrate, $\boldsymbol{F}_s$, that opposes the applied hydrodynamic drag, $\boldsymbol{F}_d$. The cell remains stationary until the drag exceeds an unknown maximum static friction threshold, $F_{s,max}$:

$$\dot{\boldsymbol{s}}_c(t) = 0 \iff \|\boldsymbol{F}_d(t)\| \leq F_{s,max}$$

Crucially, this threshold $F_{s,max}$ is not directly measurable from sensor data while the cell is static. One can only infer that its value is greater than or equal to the currently applied drag. This information gap creates a significant control challenge: the system is static until it abruptly and unpredictably transitions to a kinetic state. A control policy that is not prepared for this sudden transition risks causing an uncontrolled acceleration of the cell towards the pipette (i.e., cell loss). Therefore, the control policy should not necessarily seek to always keep $\|\boldsymbol{F}_d(t)\|$ below $F_{s,max}$, but must instead select the optimal actions after forecasting the worst-case scenario where the friction threshold is imminently breached.

To formalize this, the cell's dynamics are described by a function $\mathcal{F}$ dependent on a vector of unknown friction related physical parameters, $\boldsymbol{\theta}$, which includes $F_{s,max}$. The evolution of the cell's full kinematic state, $\boldsymbol{X}_c(t) = [\boldsymbol{s}_c(t)^T, \dot{\boldsymbol{s}}_c(t)^T]^T$, is given by:

$$\boldsymbol{X}_c(t+1) = \mathcal{F}[\boldsymbol{X}_c(t), \boldsymbol{s}_p(t), \boldsymbol{u}(t), \boldsymbol{\theta}]$$

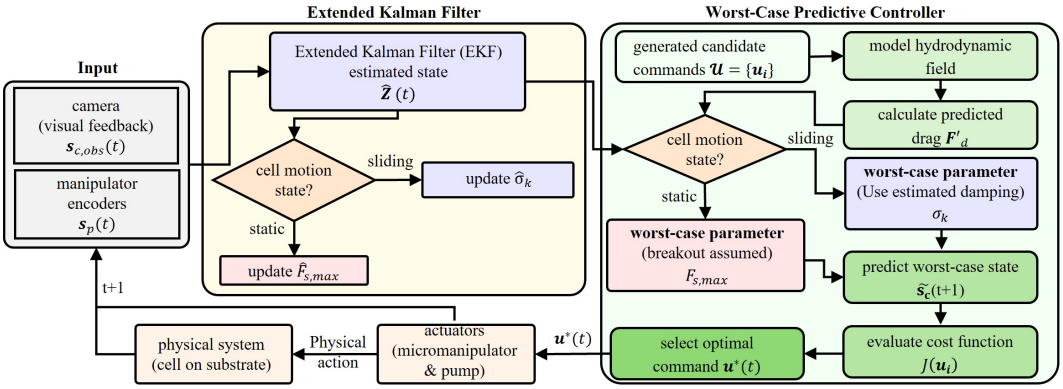

Fig. 2. The summary schematics of the proposed methodology for cell manipulation at solid-liquid interface. It consists of a modified extended Kalman Filter and a worst-case predictive controller, which is detailed in Section III.

To ensure robust operation against the uncertainty in $\boldsymbol{\theta}$, our approach evaluates each potential action against its most dangerous, physically plausible consequence. We define a function $\mathcal{W}$ to predict this worst-case state, $\tilde{\boldsymbol{X}}_c(t+1)$, by selecting the value of $\boldsymbol{\theta}$ from the current belief, $b(\boldsymbol{\theta}_t)$:

$$\tilde{\boldsymbol{X}}_c(t+1) = \mathcal{W}[\boldsymbol{X}_c(t), \boldsymbol{s}_p(t), \boldsymbol{u}(t), \boldsymbol{\theta}_{wc}(\boldsymbol{u}(t))]$$

where $\boldsymbol{\theta}_{wc}(\boldsymbol{u}(t))$ represents the worst-case parameter instantiation for a given action $\boldsymbol{u}(t)$.

This worst-case predictive model transforms the control problem into a deterministic optimization problem. A cost function, J, is formulated to penalize high-risk predicted states and reward progress. The optimal control action $\boldsymbol{u}^*(t)$ is then selected at each time step by solving:

$$\boldsymbol{u}^*(t) = \arg\min_{\boldsymbol{u}(t)\in\mathcal{U}} J(\tilde{\boldsymbol{X}}_c(t+1), \boldsymbol{u}(t))$$

where $\mathcal{U}$ is the set of admissible controls. Solving this problem requires three key components: (i) a mathematical model of the system's dynamics, (ii) a method for online estimation of the unknown parameters $\boldsymbol{\theta}$, and (iii) a predictive control law to solve the optimization. These components are detailed in the following section.

III. Methodology

To solve the formulated problem, a methodology founded upon Worst-Case Predictive Control with Online Adversarial Parameter Estimation (WPC-OAPE) is proposed. This approach is realized through three integrated components: a hybrid dynamical system model that mathematically describes the cell's behavior, a Bayesian filter for recursive estimation of states and parameters, and a predictive control law that optimizes actions against a pessimistic forecast of the system's evolution, which is summarized in Fig. 2.

A. System Dynamics Modeling

A dynamics model that describes the forces acting on the cell and its resultant motion is first established. The system's known states include the pipette position $\boldsymbol{s}_p(t)$, obtained from the manipulator's encoder, and the cell's position $\boldsymbol{s}_c(t)$, which is acquired from a custom-trained deep learning based object detection model, YOLOv11 [28].

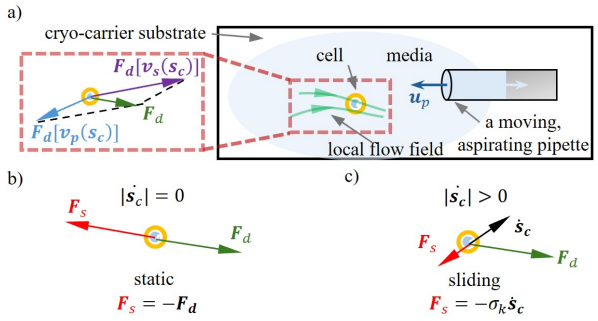

Fig. 3. Force analysis of a cell staying at liquid-solid interface. (a) For excessive liquid removal in vitrification, hydrodynamic drag force on the cell is the sum of aspiration flow and flow induced by pipette tip motion u_p. Thus, the actual drag force on the cell is the vector sum of the drag forces created by these two components. (b) Force analysis in static scenario. (c) Force analysis in sliding scenario.

The primary driving force on the cell is the hydrodynamic drag, $\boldsymbol{F}_d$, exerted by the surrounding fluid, as shown in Fig. 3a. This force is modelled using Stokes' law:

$$\boldsymbol{F}_d = 6\pi\mu R_c[\boldsymbol{v}_f(\boldsymbol{s}_c) - \dot{\boldsymbol{s}}_c] \tag{1}$$

The fluid velocity at the cell's location, $\boldsymbol{v}_f(\boldsymbol{s}_c)$, is a linear superposition of two fields: $\boldsymbol{v}_f = \boldsymbol{v}_s + \boldsymbol{v}_p$, which is the aspiration field and pipette motion induced flow field. The first component, $\boldsymbol{v}_s$, is approximated as a point sink located at the pipette tip:

$$\boldsymbol{v}_s(\boldsymbol{s}_c) = -k\frac{Q}{||\boldsymbol{s}_c - \boldsymbol{s}_p||^3}(\boldsymbol{s}_c - \boldsymbol{s}_p) \tag{2}$$

Here, k is an experimentally determined coefficient that accounts for the specific geometry of the pipette tip, which influences the flow pattern. While this model assumes an isotropic velocity field, which simplifies the true anisotropic nature of the flow, it serves as a valid and computationally efficient approximation for control purposes as the cell predominantly resides near the pipette centerline where the model is most accurate. The second component, $\boldsymbol{v}_p$, is the velocity field induced by the motion of the pipette itself at velocity $\boldsymbol{u}_p$, which is modeled as a moving point force in a viscous fluid,

$$\boldsymbol{v}_p(\boldsymbol{s}_c) = \frac{3R_p}{4}\left(\frac{\mathbf{I}}{||\boldsymbol{d}||} + \frac{\boldsymbol{d}\boldsymbol{d}^T}{||\boldsymbol{d}||^3}\right)\boldsymbol{u}_p \tag{3}$$

where R_p is the effective radius of the pipette, $\boldsymbol{d} = \boldsymbol{s}_c - \boldsymbol{s}_p$ is the displacement vector from the pipette to the cell. In contrast to computationally prohibitive methods like computational fluid dynamics [29], this analytical model allows for rapid evaluation within the control loop. Unmodeled hydrodynamic deviations, caused by droplet shrinkage, edge proximity, and the isotropic assumption, are designed to be compensated by the safety margin intrinsic to the conservative nature of the WPC-OAPE framework.

The interaction between the cell and the substrate introduces a strong non-linearity due to friction, resulting in hybrid system dynamics. The acceleration of a cell with a mass of m, $\ddot{\boldsymbol{s}}_c$, is governed by a switched model dependent on the applied forces and its current velocity as,

$$\ddot{\boldsymbol{s}}_c = \begin{cases} \mathbf{0}, \text{ if } ||\boldsymbol{F}_d|| < F_{s,max} \text{ and } ||\dot{\boldsymbol{s}}_c|| = 0 \\ \frac{1}{m}(\boldsymbol{F}_d - \sigma_k \dot{\boldsymbol{s}}_c), \text{ otherwise} \end{cases} \tag{4}$$

where $F_{s,max}$ is the static friction threshold, and σ_k is an effective kinetic damping coefficient. The first case in Eq.(4) defines the "static" regime, as shown in Fig. 3b, where the drag force is insufficient to overcome static friction. The second case in Eq.(4) describes the "sliding" regime, as shown in Fig. 3c, where the net force dictates the acceleration. These adversarial parameters ($F_{s,max}$ and σ_k) are estimated and updated regarding to different regime, respectively.

B. State and Parameter Estimation via Extended Kalman Filter

To operate the controller, the system requires knowledge of the cell's full kinematic state ($\boldsymbol{s}_c, \dot{\boldsymbol{s}}_c$) and the friction parameters. An Extended Kalman Filter (EKF) is employed to recursively estimate these quantities from the stream of cell position measurements. The EKF is selected as it provides a robust framework for estimation in nonlinear systems, which is the case here due to the dynamics in Eq. (4). While more advanced filters like the Unscented Kalman Filter (UKF) [30] or Particle Filters [31] could potentially offer higher accuracy for severely nonlinear systems, the EKF represents a well-established balance between performance and computational efficiency [32], making it highly suitable for real-time implementation. The EKF maintains a probabilistic belief over an augmented state vector $\boldsymbol{Z}_t = [\boldsymbol{s}_{c,t}^T, \dot{\boldsymbol{s}}_{c,t}^T, F_{s,max,t}, \sigma_{k,t}]^T$.

The process model $\boldsymbol{f}$ predicts the evolution of the augmented state based on the switched dynamics, obtained via Euler integration over a time step Δt:

$$\boldsymbol{Z}_{t+1} = \boldsymbol{f}(\boldsymbol{Z}_t, \boldsymbol{u}_t) = \begin{bmatrix} \boldsymbol{s}_{c,t} + \dot{\boldsymbol{s}}_{c,t}\Delta t \\ \dot{\boldsymbol{s}}_{c,t} + \ddot{\boldsymbol{s}}_{c,t}\Delta t \\ g(F_{s,max,t}) \\ h(\sigma_{k,t}) \end{bmatrix} \tag{5}$$

where $g(\boldsymbol{.})$ and $h(\boldsymbol{.})$ is the state update function for $F_{s,max}$ and σ_k, respectively. In the EKF's prediction step, the state estimate and its covariance are propagated forward:

$$\hat{\boldsymbol{Z}}_{t+1|t} = \boldsymbol{f}(\hat{\boldsymbol{Z}}_{t|t}, \boldsymbol{u}_t) \tag{6}$$

$$\boldsymbol{P}_{t+1|t} = \boldsymbol{F}_t \boldsymbol{P}_{t|t} \boldsymbol{F}_t^T + \boldsymbol{Q}_t \tag{7}$$

where $\boldsymbol{F}_t$ is the process model Jacobian and $\boldsymbol{Q}_t$ is the process noise covariance. A key aspect of this filter is its ability to adapt its estimation strategy based on the cell's dynamic state. When the cell is static, the observation that it withstands the current drag force $\|\boldsymbol{F}_d(t)\|$ provides an inequality constraint on the static friction. The filter incorporates this information through a rectification step:

$$\hat{F}_{s,max,t+1|t} = \boldsymbol{g} = \max(\hat{F}_{s,max,t}, \|\boldsymbol{F}_d(t)\|) \tag{8}$$

This rectification is a critical modification to the standard EKF formulation. Traditional estimation techniques often require persistent excitation (i.e., continuous motion) to identify parameters. Our approach uniquely leverages information from the static phase, allowing the filter to refine its estimate of the static friction threshold even when the cell is not moving. Conversely, the kinetic damping parameter σ_k is only estimated and updated during periods of motion:

$$\hat{\sigma}_{k,t+1|t} = \boldsymbol{h} = \frac{\boldsymbol{F}_d(t) - m\ddot{\boldsymbol{s}}_c}{\dot{\boldsymbol{s}}_{c,t+1|t} + \epsilon} \tag{9}$$

where ϵ is a small constant to prevent division by zero. This dual approach ensures that all available information, from both static and kinetic observations, is leveraged for parameter estimation.

C. Worst-Case Predictive Controller

The control action is selected through a predictive optimization framework that ensures robust performance by planning against a pessimistic future (potential cell loss). Different from using reactive control methods such as Control Barrier Function [33], the proposed design allows the controller to be proactive, anticipating future states and explicitly handling constraints.

The action space is first discretized, which transforms the decision-making process into a tractable optimization problem, thus enabling an efficient search for the optimal action within a finite decision space. The set of candidate pipette velocities, $\mathcal{U}_p$, is formed by sampling uniformly distributed directions around the pipette with an interval n (positive integer), scaled by a preset velocity u_{set}, and including a zero-velocity option:

$$\mathcal{D} = \{[\cos(\frac{2\pi i}{n}), \sin(\frac{2\pi i}{n})]^T \mid i = 0, 1, \ldots, n-1\} \tag{10}$$

$$\mathcal{U}_p = \{\mathbf{0}\} \cup \{u_{set} \cdot \boldsymbol{d} \mid \boldsymbol{d} \in \mathcal{D}\} \tag{11}$$

The set of candidate aspiration rates, $\mathcal{U}_Q$, consists of q discrete levels. For example, three geometrically spaced flow rates and a zero rate were used in our implementation:

$$\mathcal{U}_Q = \{0, \tfrac{1}{4}Q_{max}, \tfrac{1}{2}Q_{max}, Q_{max}\} \tag{12}$$

The complete set of candidate actions is the Cartesian product of these components: $\mathcal{U} = \mathcal{U}_p \times \mathcal{U}_Q$.

For each candidate action $\boldsymbol{u} = [\boldsymbol{u}_p^T, Q]^T \in \mathcal{U}$, a worst-case future cell state is predicted. This pessimistic design philosophy is central to preventing cell loss. The prediction is grounded in the physics of the low Reynolds number ($Re \ll 1$) regime, where viscous forces dominate over inertia. The

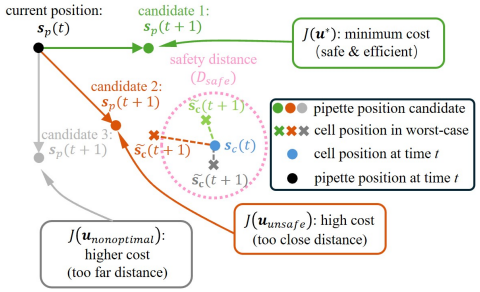

Fig. 4. Conceptual illustration of the proposed worst-case predictive control. Three candidate actions are evaluated from the current state. Candidate 1 (optimal, green) balances safety and efficiency. Candidate 2 (unsafe, orange) is penalized for violating the safety distance D_{safe}. Candidate 3 (non-optimal, grey) has a higher cost because its distance to the cell is not shortened.

prediction process unfolds in three stages: determining the breakout condition, establishing the resulting terminal velocity, and predicting the final displacement.

In the first stage, the future pipette position $\boldsymbol{s}_p(t+1)$, the future fluid velocity at cell position $\boldsymbol{v}'_f$, the prospective hydrodynamic drag force $\boldsymbol{F}'_d$ are calculated:

$$\boldsymbol{s}_p(t+1) = \boldsymbol{s}_p(t) + \boldsymbol{u}_p \Delta t \tag{13}$$

$$\boldsymbol{v}'_f = \boldsymbol{v}_f(\boldsymbol{s}_c(t)), \boldsymbol{s}_p(t+1), \boldsymbol{u}) \tag{14}$$

$$\boldsymbol{F}'_d = \boldsymbol{F}_d(\boldsymbol{s}_c(t), \boldsymbol{s}_p(t+1), \boldsymbol{u}) \tag{15}$$

The magnitude of this prospective force, $||\boldsymbol{F}'_d||$, is used to evaluate the breakout condition by comparing it to the estimated static friction threshold, $\hat{F}_{s,max,t}$.

In the second stage, the cell's resultant motion is determined. In this viscosity-dominated regime, any net force results in the cell almost instantaneously (acceleration time $\tau \approx m/(6\pi\mu R_c) << \Delta t$) reaching a terminal velocity, rather than undergoing sustained acceleration [34]. If a breakout occurs ($||\boldsymbol{F}'_d|| > \hat{F}_{s,max,t}$), the cell's terminal velocity will eventually reach the local fluid velocity, $\boldsymbol{v}'_f$. If the cell is sliding, the cell's terminal velocity is dictated by the balance between the fluid drag and the kinetic damping. The worst-case future cell velocity, $\tilde{\boldsymbol{v}}_c(t+1)$ for different conditions, is therefore defined as

$$\tilde{\boldsymbol{v}}_c(t+1) = \begin{cases} \boldsymbol{v}'_f, \text{ if } (\|\dot{\boldsymbol{s}}_c(t)\| = 0 \ \& \ \|\boldsymbol{F}'_d\| > \hat{F}_{s,max,t}) \\ \boldsymbol{0}, \text{ if } (\|\dot{\boldsymbol{s}}_c(t)\| = 0 \ \& \ |\boldsymbol{F}'_d\| \leq \hat{F}_{s,max,t}) \\ \left(\frac{6\pi\mu R_c}{\hat{\sigma}_{k,t}}\right) \boldsymbol{v}'_f, \text{ if } \|\dot{\boldsymbol{s}}_c(t)\| > 0 \end{cases} \tag{16}$$

In the third stage, the final worst-case future cell position, $\tilde{\boldsymbol{s}}_c(t+1)$, is predicted by integrating this physically-grounded worst-case velocity over the timestep:

$$\tilde{\boldsymbol{s}}_c(t+1) = \boldsymbol{s}_c(t) + \tilde{\boldsymbol{v}}_c(t+1)\Delta t \tag{17}$$

Fig. 4 conceptually illustrates this prediction process for three different candidate actions originating from the current state $[\boldsymbol{s}_c(t), \boldsymbol{s}_p(t)]$. As shown, each potential pipette movement (candidate 1, 2, and 3) results in a different worst-case prediction for the cell's future position, $\tilde{\boldsymbol{s}}_c(t+1)$.

The optimal action is selected by minimizing a cost function $J(\boldsymbol{u})$ that balances task efficiency and cell loss risk. The cost is evaluated using the predicted future states $\boldsymbol{s}'_p = \boldsymbol{s}_p(t+1)$ and $\tilde{\boldsymbol{s}}'_c = \tilde{\boldsymbol{s}}_c(t+1)$:

$$\begin{aligned} J(\boldsymbol{u}) = & -w_p(||\boldsymbol{s}_c - \boldsymbol{s}_p|| - ||\boldsymbol{s}_c - \boldsymbol{s}'_p||) \\ & + w_{safe} \cdot \text{ReLU}(D^2_{safe} - ||\boldsymbol{s}'_p - \tilde{\boldsymbol{s}}'_c||^2) \\ & + w_Q(Q_{max} - Q)^2 + w_u||\boldsymbol{u}_p||^2 \\ & + w_{smooth}||\boldsymbol{u} - \boldsymbol{u}_{prev}||^2 \end{aligned} \tag{18}$$

where w_p, w_{safe}, w_Q, w_u and w_{smooth} are positive weighting coefficients. The first term w_p rewards (negative cost) the pipette motion towards the cell for liquid removal effectiveness. This term rewards actions like candidate 1 (green path in Fig. 4) that move closer to the cell, while actions like candidate 3 (grey path), which do not try to reduce the distance to the cell and result in a higher cost. The second term w_{safe} heavily penalizes violations of a safety distance D_{safe}. This is crucial for rejecting unsafe actions, as exemplified by candidate 2 (orange path). Here, the worst-case prediction shows the pipette breaching the D_{safe} boundary, which activates the Rectified Linear Unit (ReLU) penalty [35], assigns a high cost, and thus prevents this dangerous maneuver. The last three terms w_Q, w_u, w_{smooth} regularize control effort and control smoothness. The use of a ReLU for the safety component effectively creates a soft constraint that becomes active only when the safety boundary is approached or violated, providing a strong deterrent against unsafe actions.

The action that minimizes the cost is chosen for execution:

$$\boldsymbol{u}^*(t) = \arg\min_{\boldsymbol{u} \in \mathcal{U}} J(\boldsymbol{u}) \tag{19}$$

This strategy ensures every executed action not only minimizes cell loss risk but also takes efficiency and system constraints into account. As shown in the example in Fig. 4, by evaluating the cost for all possibilities, the controller identifies that candidate 1 yields the minimum cost, selecting it as the optimal and robust action for execution.

IV. Experimental Results and Discussion

To validate the performance of our proposed WPC-OAPE control scheme, the controller was deployed into a robotic embryo vitrification system, as shown in Fig. 5a. The core of the platform is a standard inverted microscope (Nikon, Ti2-E; 2× objective, NA=0.06, depth of field ≈190 µm) equipped with a motorized XY stage for sample positioning. Fine motion control of the micropipette is achieved using a three-degree-of-freedom robotic micromanipulator (HARIOMED, IMS-320-M) with sub-micron resolution. A programmable, motor-driven microinjection pump (Eppendorf, CellTram 4 Oil) provides precise, computer-controlled command over the aspiration flow rate. As shown in 5b, the end-effector plastic micropipette (MINVITRO, MDP-135; opening ϕ = 135 µm) for oocyte and embryo manipulation, the medium (Aivfo, C006-3) and the plastic substrate-based cryo-carrier (Shengfu, SF-V01) used in the experiments are standard clinical-grade consumables, ensuring that cell-substrate interaction forces are representative of the target application. A 30 fps camera (Basler, acA1600-60gc med; pixel size 4.5

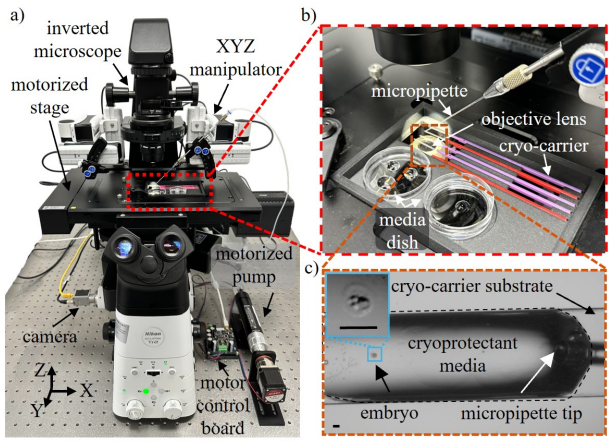

Fig. 5. System Setup. (a) The robotic cell manipulation system. (b) The module for robotic vitrification. (c) An example bottom-view image captured by the microscope camera. Scale bar: 100 µm.

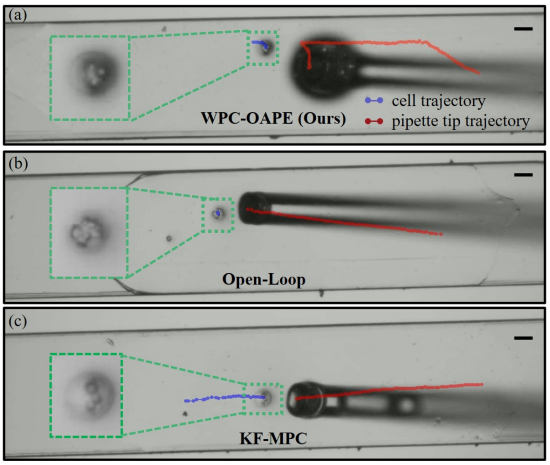

Fig. 6. Representative micropipette tip trajectories in successful trials and embryos with ideal residual media volume for (a) the proposed WPC-OAPE, (b) open-loop control, and (c) KF-MPC. Scale bar: 100 µm.

µm) provides real-time planar coordinates of the embryo's centroid (s_c) to the controller, which closes the control loop by sending velocity commands (u_p) and flow rate commands (Q) to the hardware. An example top-view image captured by the microscope camera is shown in Fig. 5c.

A. Experimental Protocol and Evaluation Metrics

To assess the proposed control scheme's ability to ensure minimal cell loss risk and effectiveness in the face of unmeasurable static friction forces, embryo manipulation experiments were performed following a standard protocol at room temperature. A micropipette dispensed a liquid droplet of approximately 1.5 µL, containing a single MII mouse embryo (Keyuebo, thawed and cultured from vitrified stock per supplier guidelines; $\phi \approx 100$ µm), onto the substrate. The assigned task was to navigate the micropipette tip towards the cell and aspirate the surrounding fluid with a $Q_{max} = 1.51$ µL/s, as is normal practice for a clinical embryologist in the vitrification process (see Fig. 6 for representative trajectories in successful trials). The task terminated when either a 8-second duration elapsed or a self-trained detection network identified an embryo with ideal residual volume for 10 consecutive image frames (zoom-in figures in Fig. 6).

Three control strategies were compared: 1) the proposed WPC-OAPE controller, 2) an open-loop controller executing a pre-programmed trajectory at a constant velocity and aspiration rate ($\frac{1}{2}Q_{max}$), and 3) a Kalman Filter-Model Predictive Control (KF-MPC) which uses a conventional Kalman Filter (estimating cell future states using kinematic data of position and velocity) and an MPC to maintain a safety distance D_{safe} from the cell during approaching using the same velocity and aspiration rate. Performance was evaluated based on: 1) success rate: a trial was successful if the self-trained detection network had identified an embryo with ideal residual volume staying on the cryo-carrier substrate for consecutive 10 frames within 8 seconds; 2) cell loss: the cell was not eventually found on the substrate; 3) execution time: for successful trials, the time from control initiation to termination. In each evaluation experiment, the same embryo was repeated used by all three strategies. Totally 30 independent experiments (30 embryos) were performed.

B. Comparative Performance Analysis

TABLE I
COMPARATIVE PERFORMANCE OF CONTROL STRATEGIES (N=30)

Methods	Trial	Success Rate (%)	Cell Loss(%)	Mean Time (s)	Max Time (s)
WPC-OAPE	(30/30)	**100**	**0**	3.6 ± 1.1	5.2
Open-loop	(20/30)	66.7	33.3	2.2 ± 0.3	2.9
KF-MPC	(25/30)	83.3	16.7	3.2 ± 0.8	4.9

The quantitative results of the comparative experiments are summarized in Table I. The proposed WPC-OAPE achieved a 100% success rate with zero cell loss. In contrast, the open-loop controller had a high failure rate of 33.3%, as its pre-programmed actions could not adapt to variations in friction, frequently causing unexpected cell aspiration into the micropipette and cell loss. The KF-MPC controller, which incorporates feedback, performed better than open-loop controllers with an 83.3% success rate.

In terms of efficiency, the open-loop controller, when successful, was the fastest (2.2 s), exploiting higher aspiration efficiency at closer proximity without safety distance constraints. A more meaningful comparison is between the two feedback controllers: the proposed WPC-OAPE (3.6 s) and the KF-MPC (3.2 s). Their execution time was comparable and not statistically different (p = 0.23). The maximum time for WPC-OAPE (5.2 s) and KF-MPC (4.9 s) was also similar, indicating that both can handle more challenging scenarios without significant delays. The slightly higher maximum time and standard deviation for WPC-OAPE were indicative of its worst-case prediction approach; it would take more time if necessary to cautiously navigate difficult friction conditions, whereas the KF-MPC might fail in those same trials. Notably, the time execution WPC-OAPE was significantly faster than that of a human operator, who typically requires 5 to 8 seconds for this task [36].

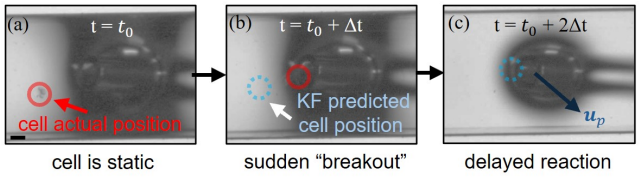

Fig. 7. Key snapshots of a typical KF-MPC failure. (a-b) The cell suddenly broke the static friction and accelerated towards the pipette. The controller's state estimate lagged reality; by the time a retreat was commanded (c), the cell was already lost. Scale bar: 100 µm.

C. Controller Behavior and Failure Case Analysis

To understand why the controllers performed differently, their behaviors were analyzed to isolate the contribution of each key concept: feedback control, adversarial parameter estimation, and worst-case predictive planning.

1) The necessity of feedback (KF-MPC vs. open-loop): The failure of the open-loop controller was straightforward: its fixed trajectory and aspiration profile are entirely blind to the cell's state. Although standard liquid dispensing protocols were used, in 33.3% of trials, this pre-programmed combination of forces exceeded the unknown static friction threshold, $F_{s,max}$, causing an uncontrolled acceleration and immediate aspiration of the cell. By adding visual feedback (the KF-MPC), the success rate increased from 66.7% to 83.3%. This demonstrates that a closed-loop system capable of reacting to the cell's observed position was essential.

2) The limits of simple kinematics-based predictive control (The KF-MPC failure cases): As a predictive controller, the KF-MPC indeed planned a trajectory by forecasting future system states. However, its predictions were derived from a purely kinematic model that only considered the cell's current, observable state: its position and velocity. As shown in Fig. 7, when the cell was stationary, the kinematic model correctly predicted that it would remain stationary. The fundamental issue was that this model was "cognitively blind" to the underlying physics of static friction. It had no conception of the hidden parameter $F_{s,max}$ or the potential for a sudden bifurcation in the system's dynamics. Consequently, the "break free" event (Fig. 7b) occurred. Once the event occurred, the controller observed the new, high-velocity state and, due to system latency, its state estimate lagged behind reality (Fig. 7b). While the MPC would attempt to re-calculate a new plan (e.g., a retreat), this re-planning was fundamentally a reaction to its own predictive failure. By the time the new plan was computed and executed, the cell was already lost (Fig. 7c). Increasing the camera frame rate reduces the state update interval and may increase success, but the unmodeled dynamics still leads to predictive failure.

3) Analysis of WPC-OAPE controller behavior: The proposed WPC-OAPE achieved a 100% success rate by developing the two components missing from the KF-MPC: static friction force inference and worst-case predictive control strategy. A typical successful trial (Fig. 8) illustrated how the two components worked in concert to proactively avoid cell loss.

WPC-OAPE was capable of extracting information from

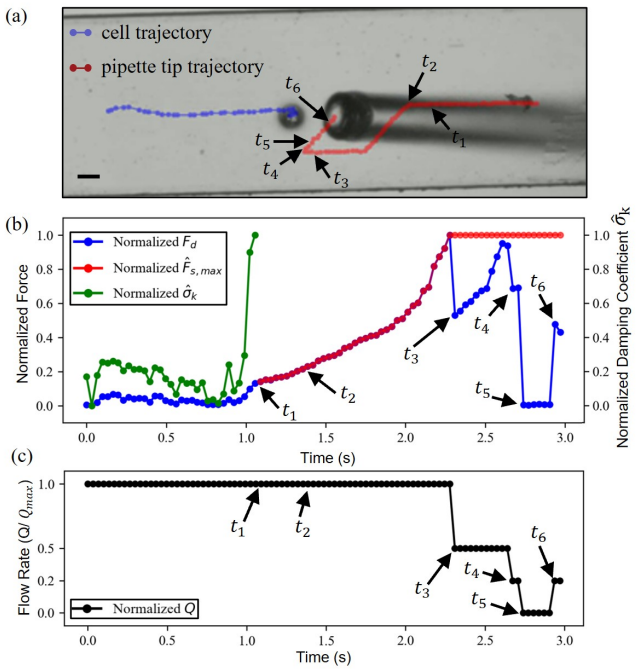

Fig. 8. Analysis of the WPC-OAPE controller's internal states during a successful trial. (a) The corresponding evolution of the controller's internal belief, showing the normalized applied drag force (F_d), the estimated static friction barrier ($\hat{F}_{s,max}$), and the estimated kinetic damping ($\hat{\sigma}_k$). (b) The discrete, normalized aspiration commands (Q) issued by the controller. (c) The final trajectory of pipette tip generated by controller. Arrows pointing to different trajectory points corresponding to the time labels in (a-b). Scale bar: 100 µm.

a static state to estimate the unmeasurable static friction force. After the cell became static at time t_1, a standard KF-MPC, being blind to the underlying system dynamics, could only predict zero future motion. In contrast, WPC-OAPE continuously computed the applied drag force F_d and leveraged it to estimate the static friction barrier, $\hat{\boldsymbol{F}}_{s,max}$, following Eq. (8), from a state that offered no kinematic information. This was reflected in Fig. 8b that $\hat{F}_{s,max}$ (red curve) rose in lockstep with the applied force (blue curve) from t_1 to t_3 as a lower-bound estimate of the friction limit.

This acquired knowledge of $\hat{F}_{s,max}$ enabled the controller to act proactively based on worst-case predictions, rather than waiting for motion to occur. The maneuver at t_2, t_3 and t_4 were direct manifestations of this preemptive strategy. Instead of acting after a breakout occurred, WPC-OAPE consistently acted to maintain an optimal state concerning the worst-case. For example, the decision to reduce aspiration was the optimal solution $\boldsymbol{u}^*$ at t_3 even the cell was static, where the cost function $J(\boldsymbol{u})$ heavily penalized any action whose worst-case would violate the cell loss constraints, calculated via Eq. (17).

Furthermore, the controller demonstrated the ability of modulating its operational strategy in different stages. The initial stage (start to t_3) was characterized by an aggressive strategy that maximized the aspiration flow rate to efficiently remove residual liquid. In contrast, the final stage (t_4 to t_6) shifted to risk-averse regulation. As the pipette operated in close proximity to the cell, the primary objective became

regulating the applied force below the established static friction limit to avoid sudden outbreak movement of cell. The fine-grained adjustments to the aspiration rate Q (Fig. 8c) were calculated to maximize fluid removal while precisely modulating the applied drag force F_d to remain safely below the estimated barrier $\hat{F}_{s,max}$ (Fig. 8b). This strategic shift ensures task completion by mitigating cell loss risk, without resorting to an overly conservative policy that could prolong the operation or cause the operation to fail.

V. Conclusion

This work handled robotic cell manipulation at a solid-liquid interface in the presence of unmeasurable static friction. During liquid removal, the unknown friction between the cell and the solid substrate may cause sudden cell acceleration and cell loss. To avoid cell loss, a worst-case predictive control with online adversarial parameter estimation (WPC-OAPE) controller was proposed. Our major contributions are a novel estimation scheme that infers the static friction barrier from a stationary cell, and the design of a worst-case predictive controller that integrates this estimate into a hybrid dynamics model to proactively pre-empt cell loss. Experimental validation on a robotic embryo vitrification system demonstrated the superiority of the proposed approach over conventional predictive controllers. The WPC-OAPE controller achieved a 100% success rate with zero cell loss. Furthermore, it completed the task with an efficiency comparable to or exceeding that of a human operator. Future work will quantify post-thaw developmental outcomes to validate the biological safety and efficacy of the method.

References

[1] Z. Zhang et al., "Robotic micromanipulation: Fundamentals and applications," *Annu. Rev. Control Robot. Auton. Syst.*, vol. 2, no. 1, pp. 181-203, 2019.

[2] W. Dou et al., "Robotic manipulation of cardiomyocytes to identify gap junction modifiers for arrhythmogenic cardiomyopathy," *Sci. Robot.*, vol. 9, no. 95, p. eadm8233, 2024.

[3] L. Königer et al., "Rebia—robotic enabled biological automation: 3d epithelial tissue production," *Adv. Sci.*, vol. 11, no. 45, p. 2406608, 2024.

[4] W. Tang et al., "Stiffening of the cytoplasm in response to intracellularly applied forces," *Nano Lett.*, vol. 24, no. 41, pp. 13085-13093, 2024.

[5] Z. Lu, et al., "Robotic ICSI (intracytoplasmic sperm injection)," *IEEE Trans. Biomed. Eng.*, vol. 58, no. 7, pp. 2102-2108, Jul. 2011.

[6] M. D'Urso et al., "Spatial regulation of substrate adhesion directs fibroblast morphotype and phenotype," *PNAS Nexus*, vol. 3, no. 8, p. pgae289, 2024.

[7] X. Wan, Z. Liu, and L. Li, "Manipulation of stem cells fates: The master and multifaceted roles of biophysical cues of biomaterials," *Adv. Funct. Mater.*, vol. 31, no. 23, p. 2010626, 2021.

[8] H. Song et al., "Automated sperm tracking and immobilization with a clinically-compatible XYZ stage," *IEEE Trans. Autom. Sci. Eng.*, vol. 22, pp. 10764-10774, 2025.

[9] B. Ní Dhonnabhain et al., "A comparison of fertility preservation outcomes in patients who froze oocytes, embryos, or ovarian tissue for medically indicated circumstances: A systematic review and meta-analysis," *Fertil. Steril.*, vol. 117, no. 6, pp. 1266-1276, 2022.

[10] A. Cobo et al., "Oocyte vitrification for fertility preservation for both medical and nonmedical reasons," *Fertil. Steril.*, vol. 115, no. 5, pp. 1091-1101, 2021.

[11] M. Ding, Z. Diao, and J. Zhou, "The preimplantation genetic testing clinical outcomes of biopsy on vitrification-warming embryos: A retrospective study," *J. Obstet. Gynaecol. Res.*, vol. 48, no. 7, pp. 1621-1631, 2022.

[12] S. Lensen et al., "The role of timing in frozen embryo transfer," *Fertil. Steril.*, vol. 118, no. 5, pp. 832-838, 2022.

[13] M. Kuwayama, "Highly efficient vitrification for cryopreservation of human oocytes and embryos: the Cryotop method," *Theriogenology*, vol. 67, no. 1, pp. 73-80, 2007.

[14] P. Mazur and S. Seki, "Survival of mouse oocytes after being cooled in a vitrification solution to -196°C at 95 to 70,000°C/min and warmed at 610 to 118,000°C/min: A new paradigm for cryopreservation by vitrification," *Cryobiology*, vol. 62, no. 1, pp. 1-7, 2011.

[15] G. Vajta, M. Kuwayama, and P. Vanderzwalmen, "Disadvantages and benefits of vitrification," in *Vitrification in Assisted Reproduction*, CRC Press, 2007, pp. 49-60.

[16] H. Liu, et al., "In situ mechanical characterization of the cell nucleus by atomic force microscopy," *ACS Nano*, vol. 8, no. 4, pp. 3821-3828, 2014.

[17] X. Wang et al., "Intracellular manipulation and measurement with multipole magnetic tweezers," *Sci. Robot.*, vol. 4, no. 28, p. eaav6180, 2019.

[18] Y. Sun and B. J. Nelson, "MEMS capacitive force sensors for cellular and flight biomechanics," *Biomed. Mater.*, vol. 2, no. 1, p. S16, 2007.

[19] X. Liu, et al., "Vision-based cellular force measurement using an elastic microfabricated device," *J. Micromech. Microeng.*, vol. 17, no. 7, p. 1281, 2007.

[20] W. Dou et al., "A microdevice platform for characterizing the effect of mechanical strain magnitudes on the maturation of iPSC-Cardiomyocytes," *Biosens. Bioelectron.*, vol. 175, p. 112875, 2021.

[21] E. Limacher et al., "Comparison of momentum and impulse formulations for PIV-based force estimation," *Meas. Sci. Technol.*, vol. 31, no. 5, p. 054001, 2020.

[22] Y. M. Kim et al., "Successful vitrification of bovine blastocysts on paper container," *Theriogenology*, vol. 78, no. 5, pp. 1085-1093, 2012.

[23] Z. Zhang et al., "Robotic pick-and-place of multiple embryos for vitrification," *IEEE Robot. Autom. Lett.*, vol. 2, no. 2, pp. 570-576, Apr. 2017.

[24] M. Lotfi, M. Nejib, and M. Naceur, "Cell adhesion to biomaterials: Concept of biocompatibility," in *Advances in Biomaterials Science and Biomedical Applications*, R. Pignatello, Ed. InTech, 2013, ch. 8.

[25] F. Kamil et al., "A review on motion planning and obstacle avoidance approaches in dynamic environments," *Adv. Robot. Autom.*, vol. 4, no. 2, 2015.

[26] M. Schwenzer et al., "Review on model predictive control: An engineering perspective," *Int. J. Adv. Manuf. Technol.*, vol. 117, no. 5, pp. 1327-1349, 2021.

[27] R. Grandia et al., "Perceptive locomotion through nonlinear model-predictive control," *IEEE Trans. Robot.*, vol. 39, no. 5, pp. 3402-3421, Oct. 2023.

[28] R. Khanam and M. Hussain, "Yolov11: An overview of the key architectural enhancements," *arXiv preprint arXiv:2410.17725*, 2024.

[29] M. H. Zawawi, et al., "A review: Fundamentals of computational fluid dynamics (CFD)," in *AIP Conference Proceedings*, vol. 2030, no. 1, AIP Publishing LLC, 2018, p. 020252.

[30] E. A. Wan and R. Van Der Merwe, "The unscented Kalman filter for nonlinear estimation," in *Proc. IEEE 2000 Adaptive Systems for Signal Processing, Communications, and Control Symposium*, 2000, pp. 153-158.

[31] P. M. Djuric et al., "Particle filtering," *IEEE Signal Process. Mag.*, vol. 20, no. 5, pp. 19-38, Sep. 2003.

[32] S. Konatowski, P. Kaniewski, and J. Matuszewski, "Comparison of estimation accuracy of EKF, UKF and PF filters," *Annu. Navig.*, vol. 23, pp. 69-87, 2016.

[33] A. D. Ames et al., "Control barrier functions: Theory and applications," in *Proc. 18th Eur. Control Conf.*, 2019, pp. 3420-3431.

[34] J. Happel and H. Brenner, *Low Reynolds Number Hydrodynamics: With Special Applications to Particulate Media*, vol. 1. Springer Science & Business Media, 2012.

[35] V. Nair and G. E. Hinton, "Rectified linear units improve restricted boltzmann machines," in *Proc. 27th Int. Conf. Mach. Learn. (ICML-10)*, 2010, pp. 807-814.

[36] A. Cobo, A. Coello, J. Remohí, J. Serrano, J. M. de Los Santos, and M. Meseguer, "Effect of oocyte vitrification on embryo quality: time-lapse analysis and morphokinetic evaluation," *Fertil. Steril.*, vol. 108, no. 3, pp. 491-497, Sep. 2017.